



Titre: Solid-liquid rotary kilns: An experimental and CFD-DEM study
Title:

Auteurs: Toni El Geitani, & Bruno Blais
Authors:

Date: 2023

Type: Article de revue / Article

Référence: El Geitani, T., & Blais, B. (2023). Solid-liquid rotary kilns: An experimental and CFD-DEM study. Powder Technology, 430, 119008 (14 pages).
Citation: <https://doi.org/10.1016/j.powtec.2023.119008>

 **Document en libre accès dans PolyPublie**
Open Access document in PolyPublie

URL de PolyPublie: <https://publications.polymtl.ca/56360/>
PolyPublie URL:

Version: Version finale avant publication / Accepted version
Révisé par les pairs / Refereed

Conditions d'utilisation: Creative Commons Attribution-Utilisation non commerciale-Pas d'oeuvre dérivée 4.0 International / Creative Commons Attribution-NonCommercial-NoDerivatives 4.0 International (CC BY-NC-ND)
Terms of Use:

 **Document publié chez l'éditeur officiel**
Document issued by the official publisher

Titre de la revue: Powder Technology (vol. 430)
Journal Title:

Maison d'édition: Elsevier B.V.
Publisher:

URL officiel: <https://doi.org/10.1016/j.powtec.2023.119008>
Official URL:

Mention légale:
Legal notice:

Solid-Liquid Rotary Kilns: An Experimental and CFD-DEM Study

Toni El Geitani^a, Bruno Blais^{a,*}

^a*Research Unit for Industrial Flows Processes (URPEI), Department of Chemical Engineering, École Polytechnique de Montréal, PO Box 6079, Stn Centre-Ville, Montréal, QC, Canada, H3C 3A7*

Abstract

Experiments for the validation of unresolved CFD-DEM software for solid-liquid flows are often expensive, time consuming and generally provide little insight into the local particles dynamics. Additionally, several DEM parameters such as the particle surface properties are often obtained from experiments in air and used for all CFD-DEM simulations even when the fluid is a liquid. We design and perform a simple and time efficient gas-solid and liquid-solid rotary kiln benchmark for the purpose of creating a validation case for unresolved CFD-DEM software which we use to validate the unresolved CFD-DEM model of the open-source software Lethe. This case, which contains dense solid-solid contacts and strong solid-fluid forces gives insight on the importance of proper calibration of DEM surface properties in solid-liquid flows as well as on the importance of the lift force. Furthermore, it is highly sensitive to the accuracy of the CFD discretization.

Keywords: Rotary kilns, Unresolved CFD-DEM, FEM-DEM, Multiphase flow.

*Corresponding author

Email address: bruno.blais@polymtl.ca (Bruno Blais)

1. Introduction

The popularity of computational fluid dynamics coupled with the discrete element method (CFD-DEM) has been increasing over the last few decades due to its accuracy in modelling multiphase solid-fluid flows [1, 2, 3]. Nevertheless, the user defined parameters that need to be inputted before a simulation can be run are numerous and an appropriate choice of these parameters is vital to obtain accurate and physically-realistic results.

Among these parameters, the choice of particle-fluid interactions plays an important role in the correct prediction of solid-fluid flows. Traditionally, CFD-DEM simulations focus mainly on the following forces: gravity and buoyancy, drag force, pressure gradient force, and shear force. The lift force is sometimes applied and sometimes neglected depending on the application being simulated. In general, in modelling solid-gas flows such as gas fluidized and spouted beds, the lift force is entirely neglected as it is considered to be of negligible magnitude compared to the dominant drag force. This is not true in solid-liquid flows. This has been demonstrated by Ferreira et al. [4] where enabling the Saffman lift force allowed for better prediction of liquid fluidized beds since the pluming effect of the particles at the top of the bed significantly diminished as a result of reduced channelling due to Saffman lift. As such, it is important to correctly choose particle-fluid interactions.

On the other hand, the DEM parameters, specifically those related to the solid particles are among the most important parameters that should be chosen carefully. In general, they include material properties and surface properties. Material properties are those related directly to the material from which is made the particles and walls such as the density, Young's modulus, and Poisson's ratio. Surface properties include the rolling and sliding friction coefficients as well as the coefficient of restitution. The latter are usually calibrated based

on the surface of dry particles. In other words, experiments are performed in air and the parameters are deduced. These dry parameters are then used for solid-liquid CFD-DEM simulations. This is the case for most modelling work done and, often, no specifications about the source of these parameters is given. Blais and Bertrand [5] found that DEM surface parameters such as the sliding and rolling friction coefficients and the coefficient of restitution play a role in the dynamics of solid-liquid flows. However, a thorough clarification about this topic and the true effect of the choice of such parameters has not been fully addressed in the literature.

It is unrealistic and unreliable to work solely with the parameters obtained from dry experiments as these particle properties tend to change when the state of the fluid changes. For example, a particle, upon hitting the ground, will usually bounce more in air than it would in water. Therefore, the coefficient of restitution of the particle is larger in dry settings than it would be in wet settings. This has been demonstrated by Joseph et al [6] where a bouncing particle experiment showed that the particle coefficient of restitution decreases with an increase in the viscosity of the fluid in which it is bouncing due to lubrication forces. The decrease becomes sharp for higher viscosities.

In the literature, the calibration of DEM properties has been mainly performed for dry materials such as the calibration of DEM parameters of cohesive bulk material using an angle of repose test [7] and the calibration of DEM properties of sticky adhesive powders for the simulation of segregation [8]. The influence and effects of the microscopic DEM parameters is discussed by Groger and Katterfeld [9] where they explain the need for the development of new calibration methods. Other researchers developed bench-scale experiments to calibrate and investigate DEM parameters such as the sliding and rolling friction coefficients, the coefficient of restitution, and the inter-particle cohesion forces

55 from the presence of liquid bridges [10]. To the knowledge of the authors, the calibration of DEM properties for solely solid-liquid simulations has not been addressed in the literature.

There exist several experiments that allow the deduction of such parameters. Among them, we mention rotary kiln experiments where a lab-scale cylindrical
60 bed is filled with particles, or a combination of particles and a fluid are allowed to rotate. Depending on the velocity of the rotation, the flow regime inside the rotary kiln changes. This change is often determined by the rotational Froude number [11]. This dimensionless number is defined as the ratio of centrifugal forces to gravity and is given by the following [11]:

$$Fr = \frac{\omega^2 R}{g} \quad (1)$$

65 where ω is the kiln rotational velocity in rad s^{-1} , R is the kiln radius in m, and g is the gravity in m s^{-2} . For a specific range of Froude numbers, the particles exhibit a certain regime inside the rotary kiln. Fig. 1 demonstrates the different regimes that can be observed in a rotary kiln as a function of the Froude number.

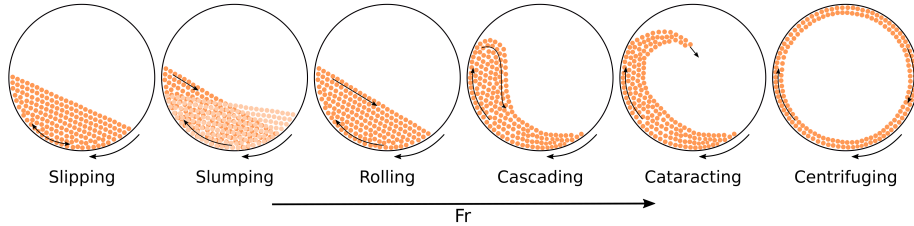


Figure 1: Particles flow regimes in rotary kilns as a function of Froude number. Reproduced from [12].

70 Increasing the Froude number allows the flow to transition from one regime to another. It is not necessary that all flow regimes are exhibited for every

experiment. Sometimes, the flow transitions from one regime to another while skipping a certain regime. This is because the velocity range for the skipped regime is so small that it is not captured during the experiment. The regime
75 at the lowest rotational speed is the slipping regime where particles slip along the wall of the bed and they can be seen to barely move. The slumping regime comes next where the particle bed behaves like a see-saw with the bed moving in an up and down motion. At higher rotational speeds is the rolling regime where particles start moving along the wall and then roll downwards after reaching the
80 top of the packing. The cascading regime occurs when the surface layer arches resulting in a crescent shape. The cataracting regime results when particles start to be thrown away into free space, falling into the bed of particles and then reattaching towards the base in a cascading motion. The centrifuging regime occurs when the $Fr > 1$, meaning that the centrifugal forces outweigh
85 the gravitational forces. The particles adhere to the wall of the kiln and perform full rotations.

It is important to note that the Froude number is not always very reliable in determining the regime change intervals because even for a constant Froude number, the behavior of the drum can be affected by the volumetric fill level
90 of the kiln and the friction coefficients between the kiln wall and the particles [12]. For example, filling the kiln to lower levels or increasing the sliding friction coefficient can lead to more cataracting or centrifuging motion. Additionally, the Froude number is determined based on the particles motion in air. There is no mentioning of the effect of different fluids on the Froude interval for the
95 regime change of the flow. This is because the gravity in the fluid is countered by the buoyancy force and as such it is expected that a new weaker gravitational acceleration should be considered in Eq. 1 when the fluid inside the kiln is a liquid. Furthermore, the Froude number does not take into account the fluid

viscosity and therefore, on its own, it can not be used as a measure for regime
100 change with fluids of high viscosities.

In general, not many studies of solid-liquid rotary kilns have been performed
in the literature. Many researchers experimentally studied the mixing of solid
materials in air inside a rotary kiln and investigated the effects of particle types
and densities, kiln loading, rotational speed and wall friction on the mixing rates
105 in the bed [13, 14]. Parsons et al. [15] experimentally studied the solid-liquid
mass transfer in slurries agitated inside a rotary kiln. Tang et al. [16] modelled
a three-phase gas-solid-liquid flow using CFD-DEM coupled with volume of
fluid (VOF) to study gas-solid-liquid flows and mixing behaviors in rotary kilns
taking into account inter-particle collisions, inter-phase interactions, and inter-
110 face morphology. Additionally, mills such as semi autogenous grinding (SAG)
mills, which have many similarities to solid-liquid rotary kilns in the cataract-
ing regime if breakage is ignored, are studied using either DEM [17] where rock
breakage mechanisms and the life cycle of rocks in mills are explored or CFD-
DEM [18] where a method for calculating the efficiency of the SAG process
115 based on the numerical results is proposed.

The aim of this work is to develop a simple and easily reproducible exper-
imental and computational procedure that allows the calibration of the DEM
surface properties and the validation of any unresolved CFD-DEM code for
solid-liquid flows. For this, a lab-scale rotary kiln experiment is performed
120 where different types of particles and fluids are used to calibrate the particle
and wall properties and to determine the effect of the choice of fluid on the
DEM surface properties. This experiment is chosen specifically because of its
simplicity and due to the complicated regimes exhibited by the particles in the
rotary kiln at the various rotational velocities it is subjected to.

125 2. CFD-DEM Model

In this section, the governing equations, particle-fluid interactions and DEM parameters are described briefly. No matter the type of CFD-DEM simulations, the governing equations are mainly separated into those related to the fluid phase and they are the volume-averaged Navier-Stokes (VANS) equations and
 130 those related to the solid phase and they are Newton's equation of motion and Euler's equation of angular momentum.

2.1. Fluid Phase Modelling

The VANS equations are divided mainly into two models: A and B. As we will only use model A in this work, we introduce it in this section. For
 135 further description of the two models and for a detailed discussion about their differences and similarities, we refer the reader to the article by El Geitani et al. [19]. The VANS equations are made up of the continuity equation and the momentum equation. The continuity equation is given by:

$$\frac{\partial \varepsilon_f}{\partial t} + \nabla \cdot (\varepsilon_f \mathbf{u}) = 0 \quad (2)$$

where \mathbf{u} is the fluid velocity, and ε_f is the void fraction calculated using
 140 one of many available particle projection schemes. The momentum equation is given by:

$$\rho_f \left[\frac{\partial \varepsilon_f \mathbf{u}}{\partial t} + \nabla \cdot (\varepsilon_f \mathbf{u} \otimes \mathbf{u}) \right] = -\varepsilon_f \nabla p + \varepsilon_f \nabla \cdot \boldsymbol{\tau} - \mathbf{F}_{pf} \quad (3)$$

where p is the pressure, and $\boldsymbol{\tau}$ is the shear stress tensor and is given by:

$$\boldsymbol{\tau} = \mu_f \left[(\nabla \cdot \mathbf{u}) + (\nabla \cdot \mathbf{u})^T - \frac{2}{3} (\nabla \cdot \mathbf{u}) \mathbf{I} \right] \quad (4)$$

μ_f is the dynamic viscosity, \mathbf{I} is the identity matrix and \mathbf{F}_{pf} in equation (3) is the fluid-particle interactions vector and is given by:

$$\mathbf{F}_{pf} = \frac{1}{\Delta V_\Omega} \sum_i^{N_p} (\mathbf{f}_{pf,i} - \mathbf{f}_{\nabla p} - \mathbf{f}_{\nabla \cdot \boldsymbol{\tau}} - \mathbf{f}_b) \quad (5)$$

where $\mathbf{f}_{pf,i}$ is the sum of particle-fluid interaction forces such as drag (\mathbf{f}_d), Saffman lift (\mathbf{f}_{Saff}), Magnus lift (\mathbf{f}_{Mag}), virtual mass (\mathbf{f}_{vm}), and Basset force (\mathbf{f}_B). $\mathbf{f}_{\nabla p}$ is the pressure gradient force, $\mathbf{f}_{\nabla \cdot \boldsymbol{\tau}}$ is the shear stress force, and \mathbf{f}_b is the buoyancy force. In this work, only Saffman lift (\mathbf{f}_{Saff}), Magnus lift (\mathbf{f}_{Mag}) and drag (\mathbf{f}_d) are considered for the particle-fluid interaction forces since the remaining forces are of negligible magnitude. This is because the fluid to solid density ratio is relatively small allowing to neglect the virtual mass force. Additionally, there exist no expression for these forces in the case of a swarm of particles as they were derived for individual particles.. This gives for a particle i , the particle-fluid force as:

$$\mathbf{f}_{pf,i} = \mathbf{f}_{d,i} + \mathbf{f}_{\text{Saff},i} + \mathbf{f}_{\text{Mag},i} + \mathbf{f}_{\nabla p} + \mathbf{f}_{\nabla \cdot \boldsymbol{\tau}} + \mathbf{f}_b \quad (6)$$

The particle-fluid interactions implemented in this work are summarized in Table 1 where d_p represents the particle diameter, V_p the particle volume, and \mathbf{v}_p the particle velocity.

Table 1: Implemented Particle Fluid Interactions.

Forces and Parameters	Equations
Pressure Force	$\mathbf{f}_{\nabla p} = V_p \nabla p$
Shear Force	$\mathbf{f}_{\nabla \cdot \boldsymbol{\tau}} = V_p \nabla \cdot \boldsymbol{\tau}$
Buoyancy Force	$\mathbf{f}_b = V_p \rho_f \mathbf{g}$
Drag Force	$\mathbf{f}_d = \frac{1}{2} \rho_f C_D \frac{\pi d_p^2}{4} \mathbf{u} - \mathbf{v}_p (\mathbf{u} - \mathbf{v}_p)$
Particle Reynolds Number	$Re_p = \rho_f \epsilon_f \mathbf{u} - \mathbf{v}_{p,i} d_p / \mu_f$
Drag Coefficient [20]	$C_D = \left(0.63 + \frac{4.8}{\sqrt{Re_p}}\right)^2 \mathbf{u} - \mathbf{v}_p \epsilon_f^\eta$
Saffman Lift Force [21, 22, 23]	$\mathbf{f}_{\text{Saff}} = 1.161 C_S d_p^2 (\mu_f \rho_f)^{1/2} \boldsymbol{\omega}_c ^{-1/2} [(\mathbf{u} - \mathbf{v}_p) \times \boldsymbol{\omega}_c]$
Vorticity	$\boldsymbol{\omega}_c = \nabla \times \mathbf{u}$
Saffman Lift Coefficient	$C_S = \begin{cases} (1 - \beta) e^{(-Re_p/10)} + \beta, & \text{for } Re_p \leq 40 \\ 0.0524 (\alpha Re_p)^{1/2}, & \text{for } Re_p > 40 \end{cases}$
Magnus Lift Force [24]	$\mathbf{f}_{Mag} = \frac{1}{2} \rho_f A_p C_{LR} \mathbf{v}_p - \mathbf{u} (\mathbf{v}_p - \mathbf{u})$
Magnus Lift Coefficient [25]	$C_{LR} = \frac{d_p \omega_p}{ \mathbf{u} - \mathbf{v}_p }$
Vortical Torque [26]	$\mathbf{M}_{vor} = \pi d_p^3 \mu_f (0.5 \omega_{c,i})$
Rotational Dissipation Torque [26]	$\mathbf{M}_{rot} = -\pi d_p^3 \mu_f (\omega_{p,i})$
η	$2 - \left[3.7 - 0.65 e^{-(1.5 - \log_{10}(Re_p))^2 / 2}\right]$
α	$\alpha = [d_p / (2 \mathbf{u} - \mathbf{v}_p)] \boldsymbol{\omega}_c $
β	$\beta = 0.3314 \alpha^{1/2}$

155 There exist several models for the calculation of the drag force. The drag
 model used in this work is the DiFelice drag model [20] as it is shown to give good
 results and is often used in the literature. Other drag models, such as the Rong
 drag model [27], were tested within the present work and led to similar results
 as the DiFelice model. Both the Saffman and Magnus lift forces are applied in
 160 this work. Considering the large shear rate that occurs in the vicinity of the

wall and the large particle angular velocity observed experimentally (discussed in a later section), these forces are no longer negligible in liquids and they might have an effect on the simulation results. When the Magnus lift force is applied, a rotational dissipation torque as given in Table 1 should be applied to the
165 particles. This will allow the dissipation of the particles rotational velocities and prevent them from spinning uncontrollably which can result in nonphysical values of the Magnus lift as it is proportionally dependent on the particles rotational velocities.

2.2. Solid Phase Modelling

170 The solid particles are individually tracked by integrating Newton's equation of motion and Euler's angular momentum equation. Newton's equation is:

$$m_i \frac{\partial \mathbf{v}_{p,i}}{\partial t} = \sum_{j \in C_i} \mathbf{f}_{ij} + \sum_w \mathbf{f}_{w,i} + m_i \mathbf{g} + \mathbf{f}_{fp,i} \quad (7)$$

where m_i is the mass of particle i , $\mathbf{v}_{p,i}$ is the particle i velocity, \mathbf{f}_{ij} are the contact forces between particle i and particle j , C_i includes all particles in the contact list of particle i , $\mathbf{f}_{w,i}$ are the interactions between particle i
175 and the walls where w loops over all walls in contact with particle i , \mathbf{g} is the gravitational acceleration and $\mathbf{f}_{fp,i} = -\mathbf{f}_{pf,i}$ are the interactions between the fluid and particle i which represent the coupling forces between the two phases.

The particle rotational movement is described by:

$$I_i \frac{\partial \boldsymbol{\omega}_{p,i}}{\partial t} = \sum_{j \in C_i} (\mathbf{M}_{ij}^t + \mathbf{M}_{ij}^r) + \mathbf{M}_i^{ext} \quad (8)$$

where I_i is the moment of inertia of particle i , $\boldsymbol{\omega}_{p,i}$ is the angular velocity of particle i , \mathbf{M}_{ij}^t and \mathbf{M}_{ij}^r are respectively the tangential and rolling friction

180 torques due to the contact between particles i and j , and \mathbf{M}_i^{ext} denotes all other external torques. In this work, an external torque known as viscous torque is applied as described by Derksen [26] that takes into account the fluid vorticity at the particle position (vortical torque \mathbf{M}_{vor}) and the particle angular velocity (rotational dissipation torque \mathbf{M}_{rot}). DEM is described briefly in this section.

185 For more detailed information about DEM, we refer the reader to the paper by Golshan et al. [2].

Since we are dealing with dense solid-fluid systems, the soft-sphere DEM model is used where artificial overlaps and a set of imaginary springs and dashpots are used for the modelling of contact forces and torques resulting from particle collisions. This allows for multiple collisions that last several time

190 steps and allows for overlap between the particles during collision. The particle contact force can be calculated using several contact models such as the linear visco-elastic model, non-linear visco-elastic model, and the elastic perfectly plastic models. In this work, we use a non-linear visco-elastic model. The

195 particle contact force (\mathbf{f}_{ij}) can be decomposed into its normal and tangential components as [28]:

$$\mathbf{f}_{ij} = \mathbf{f}_{n,ij} + \mathbf{f}_{t,ij} = -k_{n,ij}\boldsymbol{\delta}_{n,ij} - \gamma_{n,ij}\dot{\boldsymbol{\delta}}_{n,ij} - k_{t,ij}\boldsymbol{\delta}_{t,ij} - \gamma_{t,ij}\dot{\boldsymbol{\delta}}_{t,ij} \quad (9)$$

where k and γ are the spring stiffness and damping coefficients and are a function of the Young's modulus (Y), the coefficient of restitution (e_r), and the Poisson ratio (ν). $\boldsymbol{\delta}$ is the overlap, and $\dot{\boldsymbol{\delta}}$ is the time derivative of the

200 overlap which represents the velocity. The tangential overlap $\boldsymbol{\delta}_{t,ij}$ is limited by Coulomb's criterion [28]:

$$\boldsymbol{\delta}_{t,ij} \leq -\mu_{d,ij} |\mathbf{f}_{n,ij}| \frac{\boldsymbol{\delta}_{n,ij}}{|\boldsymbol{\delta}_{n,ij}|} \quad (10)$$

where μ_d is the coefficient of dynamic friction [28]. The tangential, rolling, and viscous torques are obtained as:

$$\mathbf{M}_{t,ij} = \mathbf{r}_i \times (\mathbf{f}_{ct,ij}) \quad (11)$$

$$\mathbf{M}_{r,ij} = -\mu_{r,ij} |\mathbf{f}_{ct,ij}| \frac{\boldsymbol{\omega}_{p,ij}}{|\boldsymbol{\omega}_{p,ij}|} R_{e,ij} \quad (12)$$

$$\mathbf{M}_{viscous,i} = \pi d_p^3 \mu_f \left(\underbrace{0.5\omega_{c,i}}_{\mathbf{M}_{vor}} - \underbrace{\omega_{p,i}}_{\mathbf{M}_{rot}} \right) \quad (13)$$

where $\mu_{r,ij}$ is the coefficient of rolling friction, $R_{e,ij}$ is the effective radius, \mathbf{r}_i is the distance between particle i and the contact point, and $\boldsymbol{\omega}_{p,ij}$ is the relative angular velocity of particle i with respect to particle j . In this work, only the rotational dissipation torque portion of the viscous torque is enabled to allow for the dissipation of the particle angular velocity and prevent unrealistic values of the Magnus lift force. The vortical torque is not applied as the fluid vorticity is deemed to be not sufficiently resolved to obtain realistic and stable results.

The necessary DEM parameters and their respective equations are given in Table 2.

Table 2: Normal and tangential spring and damping constants for the visco-elastic model.

Parameters	Equations
Normal spring constant	$k_n = \frac{4}{3}Y_e\sqrt{R_e\delta_n}$
Normal damping coefficient	$\gamma_n = -2\sqrt{\frac{5}{6}}\beta\sqrt{S_n m_e}$
Tangential spring constant	$k_t = 8G_e\sqrt{R_e\delta_n}$
Tangential damping coefficient	$\gamma_t = -2\sqrt{\frac{5}{6}}\beta\sqrt{S_t m_e}$
Effective mass	$\frac{1}{m_e} = \frac{1}{m_i} + \frac{1}{m_j}$
Effective radius	$\frac{1}{R_e} = \frac{1}{R_i} + \frac{1}{R_j}$
Effective shear modulus	$\frac{1}{G_e} = \frac{2(2-\nu_i)(1+\nu_i)}{Y_i} + \frac{2(2-\nu_j)(1+\nu_j)}{Y_j}$
Effective Young's modulus	$\frac{1}{Y_e} = \frac{(1-\nu_i^2)}{Y_i} + \frac{(1-\nu_j^2)}{Y_j}$
β	$\beta = \frac{\ln e}{\sqrt{\ln^2 e + \pi^2}}$
S_n	$S_n = 2Y_e\sqrt{R_e\delta_n}$
S_t	$S_t = 8G_e\sqrt{R_e\delta_n}$

The DEM time step is commonly chosen to be between 10 % and 20 % of the critical time step (Δt_{crit}) required for stability of the DEM simulation. To
215 calculate the critical time step, the Rayleigh characteristic time is used where the smallest Rayleigh time step among all particles is taken to be the critical time step. It is determined as [29, 28]:

$$\Delta t_{crit} = \min_{i \in N_p} \left(\frac{\pi r_i}{0.1631\nu_i + 0.8766} \sqrt{\frac{\rho_i}{G_i}} \right) \quad (14)$$

where N_p is the total number of particles, ρ_i is the particle density, G_i is the particle shear modulus, ν_i is the particle Poisson's ratio, and r_i is the particle
220 radius.

3. Experimental and Simulation Setup

In the present section, the materials and experimental setup as well as the simulation parameters and setup are introduced.

3.1. Rotary Kiln Experiment

225 Several types of particles are mixed with various fluids having different densities and viscosities and made to rotate in a lab-scale rotary kiln using a rotating ball mill in an attempt to create a simple validation test case with complex fluidization regimes for CFD-DEM simulations.

3.1.1. Ball Mill Setup

230 The lab-scale rotary kiln is made from acrylic and has a removable lid on its top wall which allows its filling and emptying. The lid is fixed onto the kiln using 15 screws. Below the lid exists a water tight gasket that prevents any leakage. The rotary kiln is of cylindrical shape with a length of 0.185 m and a radius of 0.069 m . The experimental setup is shown in Fig. 2.

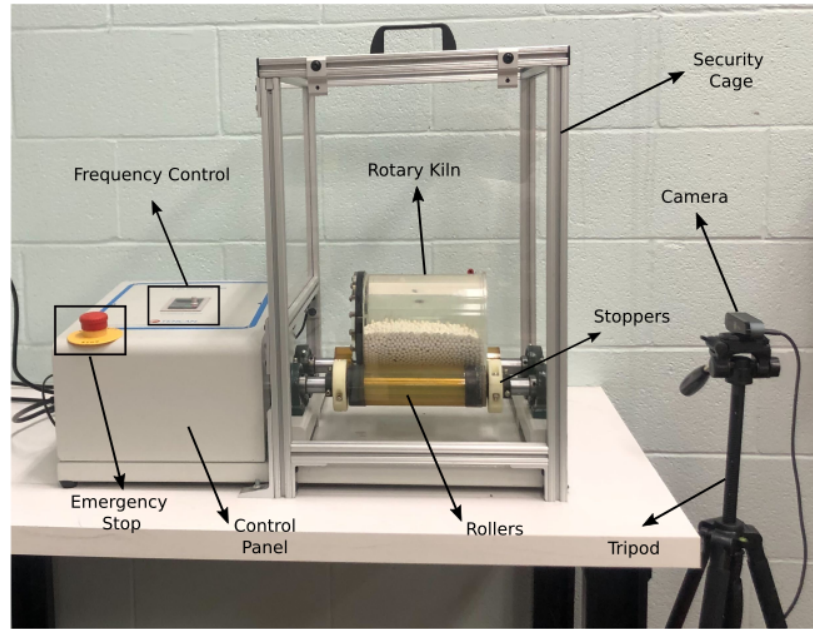


Figure 2: The experimental setup showing the rotary kiln and the rotating ball mill.

235 The water-tight rotary kiln is constructed in-house in the lab of Polytech-
 nique Montreal. It is placed on an off-the-shelf lab roll ball mill with the fol-
 lowing specifications: manufacturer Changsha Tianchuang Powder Technology
 Co., LTD, model QM-5, dimensions 70x415x260 mm, net weight 32 kg and mo-
 tor operating frequency range of 0 Hz-600 Hz. The setup is easily reproducible
 240 at a modest cost. The front roller is connected to the motor shaft located in-
 side the control panel and is the one that rotates. The back roller is a passive
 roller which is entrained by the motion of the front roller and its position can be
 changed depending on the size of the rotary kiln. The camera used is a Logitech
 Brio camera with an operating range of 30-60 frames per second.

245 3.1.2. Characteristics of the Particles

We used three types of particles to carry out the experiments: acrylonitrile
 butadiene styrene (ABS) and two sizes of glass beads which are relatively cheap

to buy. All particles are considered to be completely spherical with a sphericity
of 1 and a uniform particle size distribution. The diameter of the ABS particles
250 is 5.95 mm and their density is 1813 kg m^{-3} . The glass beads used were of
diameters 3 mm and 5 mm and a density of 2500 kg m^{-3} . The different particles
are represented in Fig. 3.

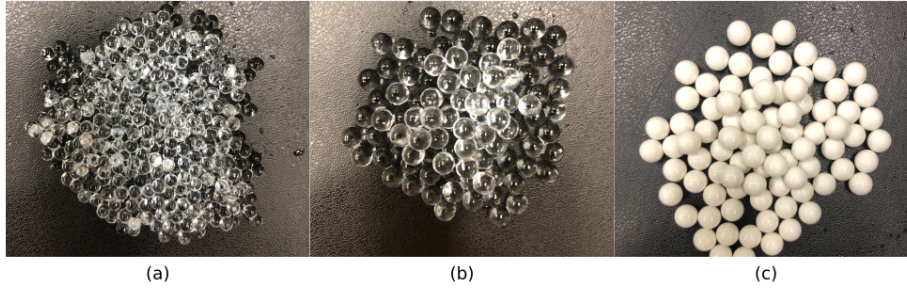


Figure 3: The different particles used in the experiment: (a) 3 mm glass beads, (b) 5 mm glass beads, and (c) 5.95 mm ABS particles.

3.1.3. *Synthesis of the Fluid*

Since the goal is to create a simple validation experiment with no complex
255 equipment, the fluids with varying viscosities used were air, water, and sucrose
aqueous solutions with 50 %, 66.66 %, and 100 % w_s/w_w sucrose to water
weight fractions. The sucrose solutions are prepared by mixing 3 L of water
corresponding to 2.991 kg with the equivalent mass of table sugar which is the
main cost related to the synthesis of the viscous solutions. The properties
260 of each fluid are shown in Table 3. The densities of the sucrose solution are
interpolated from the data tables by Cerdeirina et al. [30] while the viscosities
are interpolated from the data tables by Telis et al. [31] for a temperature of
25 °C.

	Air	Water	Sucrose Solution		
Sucrose Fraction (w_s/w_w)	0 %	0 %	50 %	66.66 %	100 %
Sugar Mass (kg)	0	0	1495.5	1993.8	2991
Fluid Mass (kg)	0	0	2991	2991	2991
Density (kg m^{-3})	1.225	997	1138.5	1175.62	1229.25
Viscosity ($\text{mPa} \cdot \text{s}$)	0.016	1	3.49	5.17	11.5

Table 3: Fluids used in the experiment and their composition.

2 L of hot water are mixed with the table sugar and stirred continuously
265 until most of the sugar is dissolved. Then, 1 L of room temperature water is
added to the mixture and stirred manually to homogenize the temperature of
the mixture and ensure all table sugar is dissolved. The mixture is left several
hours until it cools down to room temperature and the mixture color turns clear.

3.1.4. Experimental Procedure

270 Particles are emptied inside the rotary kiln until a height of packing of 6.7 cm
is reached and the fluid of choice is poured over the particles until they become
fully submerged. They are left to soak for several hours while shaking the kiln
several times during the soaking period in order to remove as many air bubbles
as possible from the particle packing. Later, the kiln is completely filled with
275 the fluid of choice. Finally, the lid of the kiln is screwed in place and the kiln
is checked for any potential leakages before being placed on the rotating ball
mill. The rotating mill is started and the velocity of rotation is controlled by
manipulating the frequency of the motor.

Frequency (Hz)	20	60	140	200	300	400	500
Velocity (rps)	0.13	0.35	0.8	1.13	1.6	2.2	2.8
Velocity ω (rad s ⁻¹)	0.8164	2.198	5.024	7.0964	10.048	13.816	17.584

Table 4: Kiln rotational velocities as a function of motor frequencies.

The studied velocities in this experiment for all particle and fluid types
280 are given in Table 4. For each frequency, the behavior of the rotating kiln is
captured using the camera where a video is recorded and snapshots of the video
are analyzed comparing them to those of the simulations.

3.2. Rotary Kiln Simulation

The simulations are carried out in Lethe [32, 33, 19, 2], an open source
285 CFD, DEM, and CFD-DEM software based on the finite element method. The
detailed parameters for the simulation setup is given in Table 5. The number of
particles is calculated based on the experimental packing height of 6.7 cm and
an average packing solid fraction of $\varepsilon_s = 1 - \varepsilon_f = 0.62$. The simulations are
run for different finite element orders (Q1-Q1, Q2-Q1, Q3-Q2, and Q4-Q3) for
290 both velocity and pressure to determine the effect of the finite element order on
the simulation results. We recall that element order p leads to $p + 1$ order of
accuracy.

The DEM time step is determined by dividing the CFD time step by the cou-
pling frequency f . The coupling is performed at each CFD time step. The first
295 order backward difference (BDF1) scheme is used for time-stepping. Lethe mod-
els turbulence using implicit Large Eddy Simulations (ILES) through the finite
element stabilized formulation of the volume-averaged Navier-Stokes equations

[33].

Table 5: Simulation parameters.

Parameter	ABS	Glass	Glass
Simulation time (s)	5	5	5
Time integration method	BDF1	BDF1	BDF1
CFD time-step (Δt_{CFD})(s)	0.01	0.005	0.01
Coupling Frequency (f)	200	100	200
Radius of the kiln (R)(m)	0.069	0.069	0.069
Length of the kiln (H_b)(m)	0.185	0.185	0.185
Mesh ($\Delta_r \times \Delta_z$)	8×10	16×20	8×10
Number of particles (N_p)	6000	45362	9490
Diameter of the particles (d_p)(mm)	5.95	3	5
Density of the particles (ρ_p)(kg m^{-3})	1813	2500	2500
Young's modulus (Y)(MPa)	2.4	3	3
Poisson ratio (ν)	0.37	0.25	0.25
VANS model type	A	A	A
Void fraction calculation scheme	QCM	QCM	QCM
Void fraction smoothing length	$2d_p$	$2d_p$	$2d_p$
Boundary conditions at the walls	Dirichlet	Dirichlet	Dirichlet
Drag model	DiFelice [20]	DiFelice [20]	DiFelice [20]
Gravity (g)(m s^{-2})	9.81	9.81	9.81

As the 3 mm particles are smaller than the other particles, the mesh used
300 for the simulation of these particles is finer than that used for the larger particles. Fig. 4 shows the difference in the mesh for the smaller and larger particle types. The mesh is chosen to better resolve the fluid closer to the particle scale; therefore, the smaller the particles, the finer the mesh should be. However,

unresolved CFD-DEM limits the size of mesh elements to around $3 d_p$. There-
 305 fore, going below this limit is not feasible as the volume averaging assumptions
 that govern the VANS equations will no longer be valid leading to inaccurate
 calculation of the void fraction and affecting the stability of the solver. This
 is why the boundary layer cannot be resolved better than it already is. One
 solution would be to use a finer mesh at the boundary but this is unfeasible
 310 in unresolved CFD-DEM because if a particle goes towards the boundary, the
 void fraction becomes incorrect for the finer mesh portion. Another solution to
 improve the resolution of the fluid near the walls would be to use wall functions,
 however we are not aware of wall-function formulations which are adequate for
 the low Reynolds number considered in this work and which take into account
 315 the effect of particles. Thus, they cannot be used in unresolved CFD-DEM. This
 is one of the reasons we propose the use of high order elements for unresolved
 CFD-DEM where the boundary is better resolved without having to refine the
 mesh since the higher order polynomials allow for a steeper velocity gradient in
 the vicinity of the walls. The CFD time step chosen for the simulations depends
 320 on the Courant-Friedrichs-Lewy (CFL) condition number for which a $CFL \lesssim 1$
 is aimed for. As the mesh for the 3 mm glass beads is refined once, that is the
 mesh elements are divided once in each direction, then the CFD time step is
 also halved once to obtain stable simulations at higher velocities. Isoparametric
 elements are used in cells close to the rotating wall to ensure consistency of the
 325 high-order finite element method.

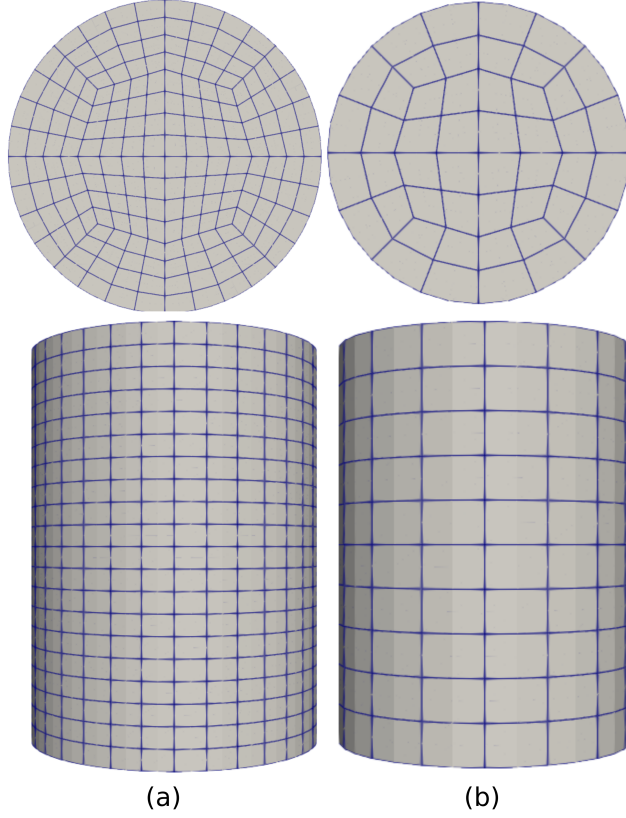


Figure 4: Top and side views of the two meshes used in the simulation for: (a) 3 mm glass beads, (b) 5 mm glass beads, and 5.95 mm ABS particles.

The void fraction is calculated using the quadrature centered method (QCM) [34] as it is an analytical method that results in a void fraction profile that is continuous in time and space. To enhance numerical stability of the VANS solver, the void fraction is smoothed using a smoothing length $L = 2d_p$ which
 330 is added to the \mathcal{L}^2 projection equation of the void fraction resulting in the following:

$$\int_{\Omega} \varphi_i \varepsilon_{f,j} \varphi_j d\Omega + \int_{\Omega} L^2 \nabla \varphi_i \nabla \varphi_j d\Omega = \int_{\Omega} \varepsilon_{f,i} \varphi_i d\Omega \quad (15)$$

where $\varepsilon_{f,i}$ and $\varepsilon_{f,j}$ are respectively the cell value and the projected nodal

value of the void fraction, and φ is the finite element basis function. We refer the reader to the article by El Geitani et al. [33] for details about the smoothing
335 strategy.

The simulation time was chosen to be 5 s to ensure that steady state has been reached inside the kiln. Multiple snapshots of the results are taken and compared to the experimental results. For the various velocities, fluids, and particle types, the sliding and rolling friction coefficients as well as the coefficient
340 of restitution are calibrated. This is done by examining the angle of inclination of particles in the kiln for the rolling flow regime and comparing the results between experiments and simulations. Moreover, the effect of these parameters on the transitioning between regimes is determined.

4. Results and Discussion

345 In this section, the experimental results are extracted and analyzed, followed by a detailed comparison between experimental and simulation results in an attempt to better understand the effect of surface parameters, particle-fluid interactions, and the order of the numerical scheme on the accuracy of predictions of CFD-DEM simulations of rotary kilns.

350 4.1. Dimensional Analysis of the System

The system is non-dimensionalized to remove all physical dimensions, resulting in a simplified and parameterized description. This clarifies the relative size and importance of the different terms and makes solving the system at different limits straightforward. The following variables are considered in the dimensional analysis of this problem: the radius of the rotary kiln (R), the diameter
355 (d_p) and density (ρ_p) of the particles, the rotational velocity (ω) of the kiln, the density (ρ_f) and viscosity (μ_f) of the fluids, and the gravitational acceleration

(g). These quantities as well as the dimensionless numbers characterizing the problem are summarized in Table 6.

Table 6: Dimensions and dimensionless numbers associated with the physical quantities for the rotary kiln.

Physical Quantities	SI Units	MLT System
R	m	L
d_p	m	L
ω	s^{-1}	T^{-1}
μ_f	$kg\ m^{-1}\ s^{-1}$	$ML^{-1}T^{-1}$
ρ_p	$kg\ m^{-3}$	ML^{-3}
ρ_f	$kg\ m^{-3}$	ML^{-3}
g	$m\ s^{-2}$	LT^{-2}
Dimensionless Numbers	Expression	
Π_1	$\frac{R}{d_p}$	-
Π_2	$\frac{\mu_f}{\rho_f d_p^2 \omega}$	-
Π_3	$\frac{\rho_p}{\rho_f}$	-
Π_4	$\frac{g}{d_p \omega^2}$	-

360 The basis of length (L), time (T), and mass (M) are taken to be d_p , ω^{-1} , and $\rho_f d_p^3$ respectively. From the dimensional analysis performed, four dimensionless numbers are obtained. Π_1 represents the size ratio between the rotary kiln and the particles. Π_2 represents $1/Re_\omega$ where Re_ω is the particle rotational Reynolds number where a new definition of velocity ωd_p is obtained. Π_3 represents the
365 density ratio between the fluids and the particles. Π_4 represents $1/Fr_p$ where the length used in Fr_p is the diameter of the particle instead of the radius of the kiln. As such, in order to determine the regime change in the rotary kiln, the dimensionless numbers considered are those that take into account the rotational

velocity of the kiln upon which the the flow regime is highly dependent.

370 4.2. Regime Change in Rotary Kiln

For varying values of Π_2 and Π_4 , the regime type has been plotted to create a map of regimes as shown in Fig. 5. For the same particle type, the regime change is dependent on both Π_2 and Π_4 where it is seen that for a given particle diameter, the relation between both dimensionless numbers and the regime change is always linear. As both Π_2 and Π_4 decrease, meaning Fr_p and Re_ω increase, the regime changes mostly from rolling to cascading. Some cases exhibit cataracting regime while others exhibit centrifuging regime as their end regimes.

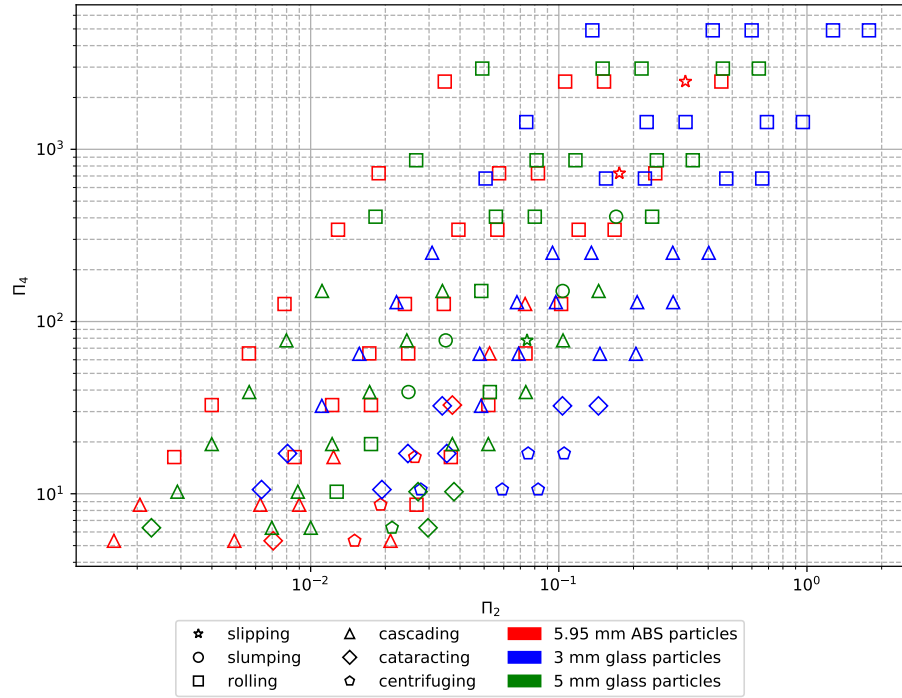


Figure 5: Rotary kiln regime map as a function of Π_2 and Π_4 .

For each particle type, the largest value of Π_2 represents the experiment with

380 air where the value of Π_3 is the smallest and the smallest value of Π_2 represent the experiment with water. The 3 mm glass particles are the only particles that exhibit centrifuging regime in air.

Additionally, for the region with a low Fr_p ($\Pi_4 > 3 \times 10^2$), the dominant regime is the rolling regime for all particle types and fluids except for 385 the 5.95 mm ABS particles at 100 % sucrose solution where a sliding regime is observed for the smallest rotational velocities. For $\Pi_4 < 3 \times 10^2$, the regime changes and evolves as a function of increasing Fr_p . The centrifuging regime is dominant at small Π_4 numbers and large Π_2 numbers which signifies that the fluid viscosity plays an important role in accelerating the regime transition. 390 Only 5 mm glass beads produce the slumping regime for 66.66 % and 100 % sucrose solutions. It is important to note that despite all efforts taken in ensuring that the rotary kiln does not slip over the rollers of the rotating ball mill, the heavier the contents of the rotary kiln are and the larger the rotational velocity is, the less certain we are that the experiments are slip free. Therefore, it might 395 be that some regimes that should have manifested in the experiment did not as an effect of the slight slip.

For most of the cases and particle-fluid combinations, the trend of the regime change is straightforward where in general the regimes follow what is shown in Fig. 1. The choice of the fluid as a liquid with varying viscosities plays a role 400 in accelerating the appearance of the regimes, that is making the same regime appear at lower rotational velocities, and in making visible some regimes that would otherwise not appear in air, specifically the sliding and slumping regimes.

4.3. Rotation of Particles in Kiln

The application of the Magnus lift force and the rotational dissipation torque 405 is valid if the particles are spinning inside the rotary kiln. To determine whether or not the particles are rotating, we mark 10 ABS particles with a black marker

on one side and a red marker on the other and place them inside the rotary kiln along with the remainder of the particles. The kiln is rotated at various rotational velocities and the results are captured using the Logitech camera.

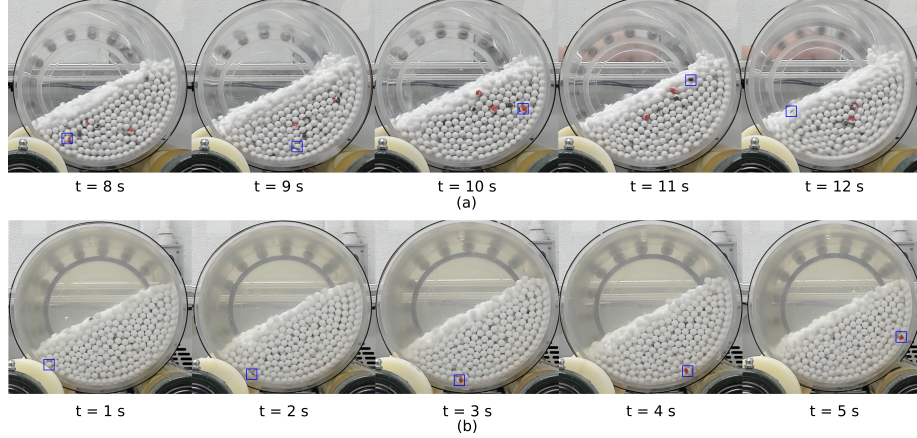


Figure 6: Snapshots of ABS particles in rotary kiln with (a) air and (b) 50 % sucrose solution where marked particles rotate considerably in a short time interval.

410 Fig. 6 demonstrate that the particles rotate significantly in both gas and liquids. As such, the application of the Magnus lift force as well as the rotational dissipation torque is justified.

4.4. Effect of the Finite Element Order on Regime Change

Different finite element orders are used in the simulation to determine the
 415 effect of accurately resolving the fluid on the regime change in the rotary kiln. For this, simulations of ABS particles and 100 % sucrose solution using Q1-Q1, Q2-Q1, Q3-Q2, and Q4-Q3 elements are run and results are compared. Fig. 7 demonstrates the regime obtained as well as the fluid boundary layer for a motor frequency of 140 Hz using the four finite element orders.

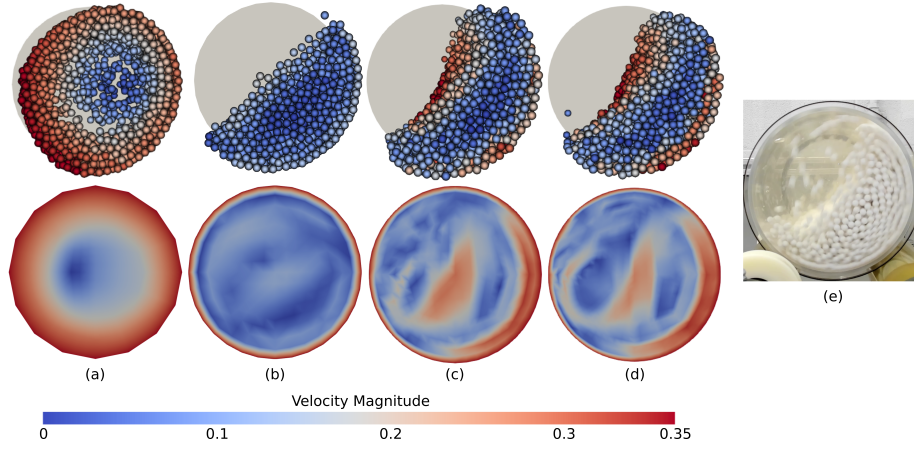


Figure 7: The regime of particle motion and the time-averaged steady-state velocity magnitude of particles and fluid as a function of finite element orders and the sliding friction coefficient for (a) Q1-Q1 and $\mu_s = 0$, (b) Q2-Q1 and $\mu_s = 0.24$, (c) Q3-Q2 and $\mu_s = 0.8$, (d) Q4-Q3 and $\mu_s = 0.8$, and the comparison with (e) experimental result.

At low rotational velocities, Q1-Q1 simulations lead to angles of inclination larger than those obtained in the experiments. Additionally, for higher velocities, it can be seen that Q1-Q1 simulations result in the wrong regime compared to the experimental result as shown in Fig. 7. This is explained by the presence of a large boundary layer equivalent to two particle diameter due to the diffusion of the fluid velocity within a cell when using Q1-Q1 elements as shown in Fig. 7 (a). This large boundary layer traps the particles at and near the wall and translates them with the same velocity as the fluid. This results in a fake centrifuging regime caused by the diffused boundary layer even for a sliding friction coefficient of 0. This is also visible looking at the fluid where a minimal velocity is observed in the center of the kiln and a maximum velocity at the boundary.

On the other hand, the low rotational velocity simulations show good agreement in the angle of inclination of the particles in the kiln between the simulation and the experimental results for Q2-Q1, Q3-Q2, and Q4-Q3 elements. However, only Q3-Q2 and Q4-Q3 simulations correctly capture and reproduce the inflec-

tion point in the middle of the inclined plane. Additionally, for higher velocities, the higher order elements lead to similar results and allow the correct regime to be obtained. This is because the boundary layer for these higher order elements is smaller than a single particle diameter as it is not as diffused as for the case of Q1-Q1 elements. As such, it is considered to move the particles correctly with a lesser effect of numerical dissipation. Nonetheless, the accuracy in resolving the fluid changes considerably between Q2-Q1, Q3-Q2, and Q4-Q3 simulations. Q3-Q2 and Q4-Q3 elements result in the most accurate predictions as shown in Fig. 7 where the fluid velocity profile is similar, contrary to Q2-Q1 simulations where the fluid velocity profile differs considerably. This translates into accurate regime prediction for the two highest orders studied.

As the element order increases and the boundary layer becomes smaller, the sliding friction coefficient in the simulations need to be increased in order to obtain correct flow regimes until it converges to a certain value and becomes independent of the order. This can be concluded from Fig. 7 where using $\mu_s = 0.24$ gives correct results for Q2-Q1 and using $\mu_s = 0.8$ gives correct results for Q3-Q2 and Q4-Q3 simulations. For Q1-Q1 simulations, no matter the value of μ_s , a complete regime change is observed where the boundary layer is large and even smaller sliding friction coefficients lead to the centrifuging regime at intermediate velocities. This means that μ_s changes between element orders as it takes into account mesh inadequacies and aims at compensating for them. Therefore, Q2-Q1 elements where μ_s is still mesh dependent, and Q3-Q2 elements where μ_s becomes mesh independent are chosen for all the simulations, because using Q4-Q3 elements has an increased computational cost with similar accuracy in the prediction of regimes, requires increased computational resources and results in large simulation times compared to using Q3-Q2 elements. It is important to mention that the calibrated data using Q2-Q1 are only valid for

Q2-Q1 and Q2-Q2 simulations but those calibrated for Q3-Q2 are valid for Q3-Q2 and all higher order elements as these properties become order independent.

465 4.5. Calibration of Surface Properties and their Effect on Regime Change

Three main particle surface properties should be calibrated for each particle type. These are the sliding friction coefficient (μ_s), the rolling friction coefficient (μ_r) and the coefficient of restitution (e_r). These parameters are calibrated by simulating the rotary kiln for each particle and fluid type at low velocities in the rolling regime and measuring the angle of inclination comparing it to the angle obtained experimentally. To determine the effect of μ_r , several simulations have been launched for the same fluid and particle types while varying only μ_r . It was found that a choice of μ_r in the range of 0.2-0.3 works well for all simulations and any change in the value within the given range has a negligible effect on the angle of inclination and at higher velocities did not play a role in the regime change. For the higher kiln rotational velocities, the choice of $\mu_r < 0.2$ affected the rotational velocity of the particles where using a $\mu_r = 0$ led to much higher rotational velocities of the particles. Therefore, since the start, we set $\mu_r = 0.2$ for all simulations of the ABS particles and $\mu_r = 0.3$ for the 3 mm and 5 mm glass beads considered in this work.

The remaining parameters requiring calibration are μ_s and e_r . μ_s was calibrated based on the angle of inclination in the rolling regime while e_r was determined as the value that allows for the centrifuging regime where possible. The calibrated values are given in Table 7 for Q2-Q1 simulations and in Table 8 for Q3-Q2 simulations.

		Fluid Type				
Particle Type	Surface Property	Air	Water	50 % Sucrose	66.66 % Sucrose	100 % Sucrose
ABS ($d_p = 5.95$ mm)	μ_s	0.3	0.24	0.24	0.24	0.24
	e_r	0.9	0.2	0.2	0.2	0.2
Glass ($d_p = 3$ mm)	μ_s	0.4	0.3	0.3	0.3	0.3
	e_r	0.97	0.2	0.2	0.2	0.2
Glass ($d_p = 5$ mm)	μ_s	0.45	0.35	0.35	0.35	0.35
	e_r	0.97	0.2	0.2	0.2	0.2

Table 7: Calibrated surface properties μ_s and e_r for Q2-Q1 simulations.

Both parameters are affected by the particle and fluid types. They change drastically when moving from air to liquid. Even though Joseph et al. [6] show that the particle coefficient of restitution decreases with an increase in the viscosity of the fluid, we find that in Q2-Q1 simulations, it decreases significantly between air and water and that for the sucrose solution with increasing viscosities, using the same e_r and μ_s as water works well. This means that in Q2-Q1 simulations, the angle of inclination as well as the regime observed are still mesh dependent. The same trend is observed for the coefficient of restitution in Q2-Q1 and Q3-Q2 simulations meaning that as long as the coefficient of restitution is small in liquids, the correct regime is obtained.

		Fluid Type				
Particle Type	Surface Property	Air	Water	50 % Sucrose	66.66 % Sucrose	100 % Sucrose
ABS ($d_p = 5.95$ mm)	μ_s	0.3	0.33	0.37	0.39	0.8
	e_r	0.9	0.2	0.2	0.2	0.1
Glass ($d_p = 3$ mm)	μ_s	0.4	0.42	0.5	0.55	0.6
	e_r	0.97	0.2	0.2	0.2	0.1
Glass ($d_p = 5$ mm)	μ_s	0.45	0.5	0.52	0.55	0.7
	e_r	0.97	0.2	0.2	0.2	0.1

Table 8: Calibrated surface properties μ_s and e_r for Q3-Q2 simulations.

However, for the sliding friction coefficient (μ_s) calibrated using Q3-Q2 simulations, the value increases with an increase in the viscosity of the fluid. This allows us to deduce that the regime change and the angle of inclination are no longer mesh dependent. The increase in the sliding friction coefficient observed
500 is explained by the lubrication force that is not explicitly applied in the unresolved CFD-DEM solver but that is compensated for by the sliding friction coefficient.

The values of μ_s and e_r shown in Tables 7 and 8 above allow for a good agreement between experimental and simulation results for all motor frequencies
505 as shown in Fig. 8 for Q2-Q1 simulations and in Fig. 9 for Q3-Q2 simulations.

Table A.9 and Table A.10 show the angle of inclination obtained through the experiments and the corresponding simulations. All dashes in the tables represent a change from the rolling regime where an angle of inclination can no longer be measured. Parity plots showing the variation of the angle of inclination
510 between the simulations and the experiments are shown in Fig. 8 for Q2-Q1 simulations and Fig. 9 for Q3-Q2 simulations.

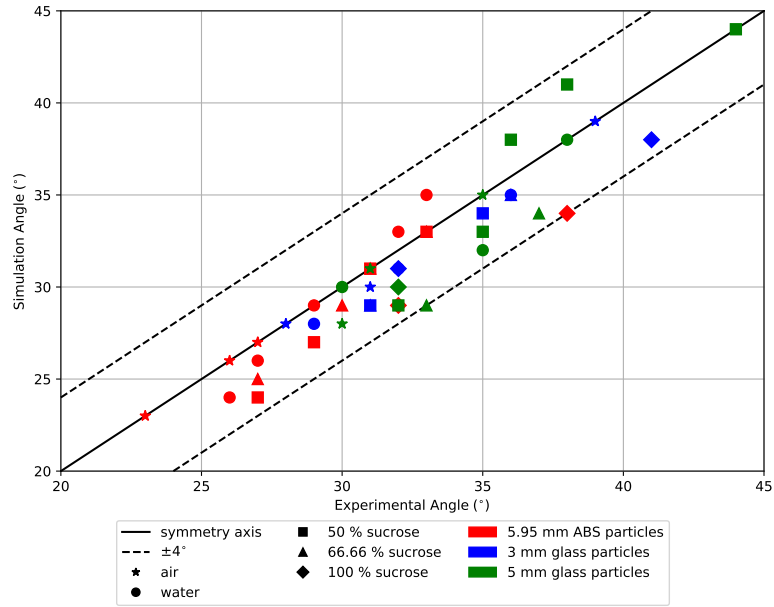


Figure 8: Comparison between the angle of inclination obtained from both experiments and Q2-Q1 simulations for all particle types.

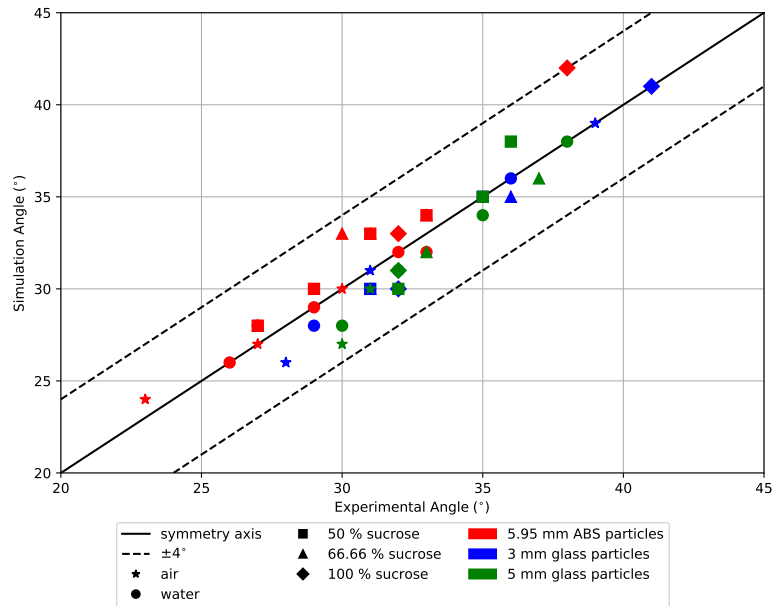


Figure 9: Comparison between the angle of inclination obtained from both experiments and Q3-Q2 simulations for all particle types.

The maximum angle difference between the simulations and experiments is of 4° while the minimum is 0° where the experiment and simulation agree 100 %. The choice of both μ_s and e_r affects the regime change in the rotary kiln. For example, in the sucrose solution where experimentally we observe the centrifuging regime, if an $e_r > 0.2$ is chosen, the particles will not centrifuge at the correct kiln velocity and will remain in the cascading or cataracting regime. Similarly, the choice of μ_s is important. If the chosen μ_s is smaller than the calibrated value, the angle of inclination would be much smaller than the experimental value and the regime change would be delayed, meaning a much higher kiln rotational velocity is required to move from one regime to the other compared to the experiment. If the chosen μ_s is greater than the calibrated value, then regimes might change much more quickly than they should and at lower kiln rotational velocities than observed experimentally. This can lead, for the same rotational velocity, to a completely different regime than the one manifested in the experiments.

Additionally, Q3-Q2 simulations show better agreement with the experimental angles of inclination compared to Q2-Q1 simulations. This is demonstrated by Fig. 9 where the points are closer to the centerline compared to those in Fig. 8. As such, Q3-Q2 simulations lead to better predictions of the angle of inclination.

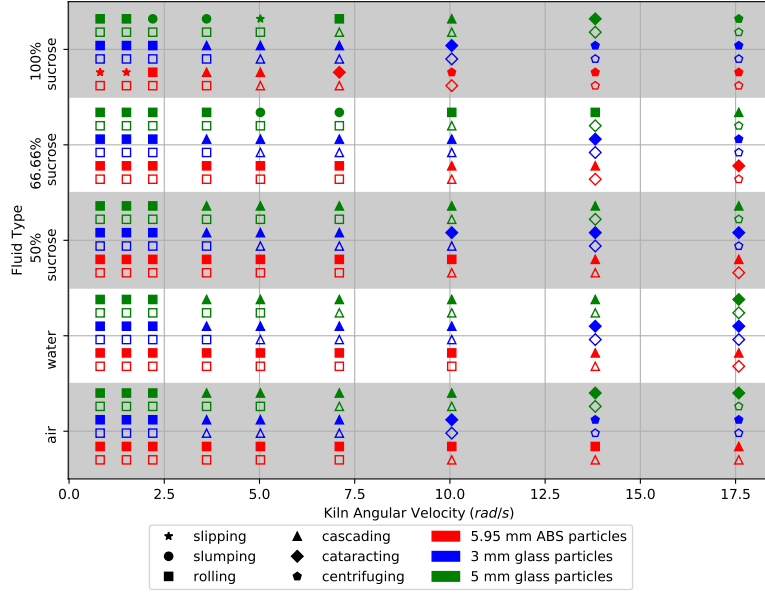


Figure 10: Comparison between the regime for experiments (filled) and Q2-Q1 simulations (hollow) at several kiln rotational speeds and for all particle types.

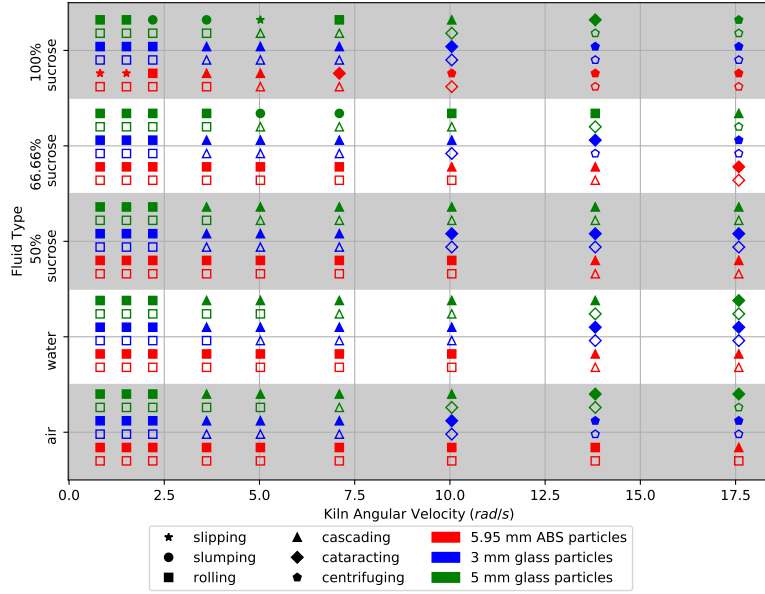


Figure 11: Comparison between the regime for experiments (filled) and Q3-Q2 simulations (hollow) at several kiln rotational speeds and for all particle types.

Figs. 10 and 11 show the regime change of the particles flow inside the kiln for the different kiln velocities of both experiments and simulations. For most of the simulations, predictions agree well with what is obtained experimentally. In some simulations, the regime change is faster than that of the experiments. This can be attributed to the slipping of the kiln on the rotating ball mill, since even slight slipping can reduce the kiln velocity and prevent the correct regime from manifesting itself. The slipping and slumping regimes observed experimentally for the 5 mm glass particles are not reproduced computationally. These regimes might have appeared experimentally due to certain particle or kiln properties that are not taken into account in the simulations. Nonetheless, the overall regime transition follows well what is observed experimentally.

We calculate the percentage accuracy of the prediction as the fraction of velocities for which the regimes agree to the total number of velocities studied for all fluid types. For Q2-Q1 simulations, the percentage accuracy of regime prediction is roughly 87 % for 3 mm glass particles, 58 % for 5 mm glass particles, and 73 % for 5.95 mm ABS particles while for Q3-Q2 simulations, the percentage accuracy of regime prediction is 96% for 3 mm glass particles, 58 % for 5 mm glass particles, and 84 % for 5.95 mm ABS particles. In general, the accuracy of regime prediction improves considerably from Q2-Q1 to Q3-Q2 simulations; however, simulations of 5 mm glass particles suffer for both orders. These particles possess the highest particle Reynolds number (Re_p) which might explain why their results are not as accurate. As such, the weak accuracy of the 5 mm glass beads for both orders means that the problem is not related to the fluid flow but can be an issue with the experimental setup or with the particles properties themselves.

4.6. *Effect of Lift Force on Regime Change*

Usually, unresolved CFD-DEM simulations account for the following forces between the solid and fluid phases: gravity including buoyancy, drag force, pressure gradient force, and shear stress force. Lift force is sometimes implemented
560 depending on the application as demonstrated by Ferreira et al. [4]. The lift force being discussed is the combination of both Saffman lift force and Magnus lift force which has a contribution to the particles translational momentum. The Saffman lift force appears when the pressure on the two sides of the particle is
565 different due to a velocity gradient in the fluid above and below the particle and thus it is termed continuous-phase vorticity-induced lift. The Saffman lift force acts in the direction from the lower relative velocity to the higher relative velocity between the particle and the fluid. The Magnus lift on the other hand is generated due to the rotation of particle and is perpendicular to the
570 direction of particle motion and fluid flow. In gaseous fluids, the lift force is usually negligible compared to the drag force. However, in liquids, lift can play an important role. Consequently, we studied the influence of the lift force on the regime transition and manifestation as a function of the kiln rotational velocity. We simulated ABS particles at a frequency of 400 Hz for a 100 % sucrose
575 solution with a combination of lift forces and with no lift force. The simulation results as well as the experimental results are shown in Fig. 12

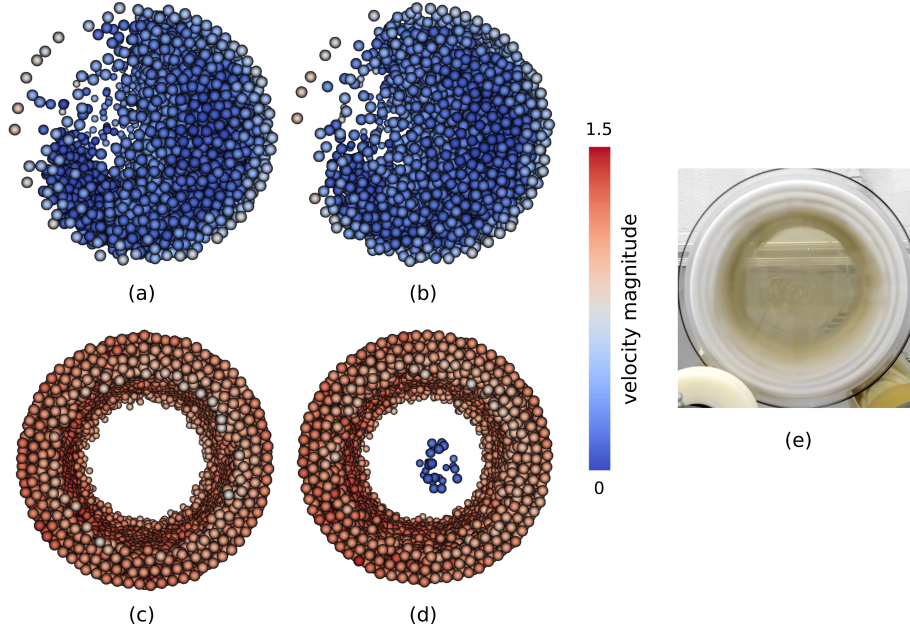


Figure 12: ABS particles flow regimes in 100 % sucrose solution at 400 Hz for Q2-Q1 simulations with: (a) no lift force, (b) Saffman lift force only, (c) Saffman and Magnus lift force and (d) Magnus lift force only, and its comparison with (e) experimental result.

In the complete absence of the lift force and in the presence of only the Saffman lift force, the particles do not centrifuge at the high velocities, which contradicts the experimental result. The simulation gives the correct regime

580 when both the Saffman and Magnus lift forces are enabled and when only the Magnus lift force is enabled. This shows that the Magnus force is the dominant component of the overall lift force at high kiln rotational velocities. According to the conclusions drawn by Loth [35], for particles with low particle Reynolds number (Re_p), the Saffman lift force dominates, while for higher Re_p , the Mag-

585 nus lift becomes substantial and might dominate the overall lift force. As such, for the rotary kiln simulation, Re_p is around 140 and thus, the Magnus lift plays an important role in the characterization of the flow regime inside the rotary kiln. This is amplified by the rotational nature of the confined flow in the kiln.

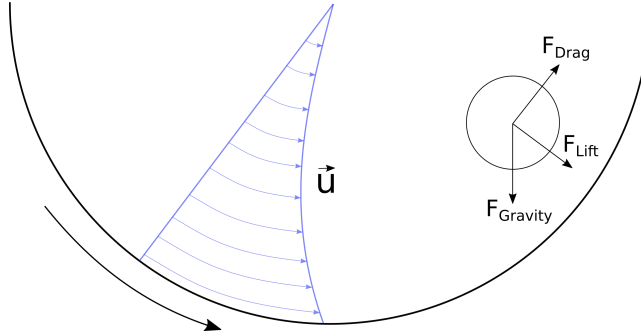


Figure 13: Forces acting on a single particle in a rotary kiln under the effect of a shear velocity flow u .

Since the fluid velocity is maximum at the wall of the rotary kiln and lower
 590 towards the center of the kiln, the lift force is expected to act perpendicular to
 the rotary kiln wall and outwards toward the wall. Fig. 13 demonstrate the
 main force balance acting on a single particle in the rotary kiln. Therefore, at
 high velocities, the lift force pushes the particles towards the wall and when it
 is large enough overcomes drag and gravity and prevents them from falling into
 595 the middle of the kiln, thus creating what is known as the centrifuging regime.

5. Conclusions

This work presents a simple and effective experimental validation bench-
 mark for unresolved CFD-DEM using a liquid-filled rotary kiln. It is a strong
 validation experiment since it exhibits many regime transitions which can be
 600 used to validate the unresolved CFD-DEM model. Another advantage of this
 experimental procedure is its simplicity, time efficiency and construction costs
 compared to other experiments used for CFD-DEM validation such as fluidized
 and spouted beds. Additionally, the different parameters and interactions that
 have a major effect on the results were analyzed and discussed. We found that
 605 the choice of particle surface properties such as the sliding friction coefficient
 and the coefficient of restitution and the order of the finite elements as well as

accounting for the different components of the lift force play an important role in determining the simulation fidelity. We proved that the particles spin around themselves inside the kiln and thus explained the importance of applying the Magnus lift in order to obtain the centrifuging regime where applicable. Finally, the rigorous validation and parameter calibration applied in this work can be used in any unresolved CFD-DEM software as it is readily reproducible. The rolling ball mill can be purchased from the manufacturer, while the cylinder can be cheaply manufactured using acrylic. The particles are commercially available, while the sucrose solution only requires table sugar for its preparation.

6. Acknowledgements

The authors would like to thank the deal.II community for their support. Bruno Blais would like to acknowledge the financial support from the Natural Sciences and Engineering Research Council of Canada (NSERC) through the RGPIN-2020-04510 Discovery Grant. The authors would also like to acknowledge technical support and computing time provided by Compute Canada and Calcul Québec.

References

- [1] Ariane Brard, Gregory S Patience, and Bruno Blais. Experimental methods in chemical engineering: Unresolved cfddem. *Canadian journal of chemical engineering*, 98(2):424–440, 2020. ISSN 0008-4034.
- [2] Shahab Golshan, Peter Munch, Rene Gassmöller, Martin Kronbichler, and Bruno Blais. Lethe-dem: An open-source parallel discrete element solver with load balancing. *Computational Particle Mechanics*, pages 1–20, 2022.
- [3] Kai Lv, Fanfei Min, Jinbo Zhu, Bao Ren, Xuejie Bai, and Chuanzhen Wang. Experiments and cfd-dem simulations of fine kaolinite particle sedimenta-

- tion dynamic characteristics in a water environment. *Powder Technology*, 382:60–69, 2021. ISSN 0032-5910. doi: <https://doi.org/10.1016/j.powtec.2020.12.057>. URL <https://www.sciencedirect.com/science/article/pii/S0032591020312249>.
635
- [4] Victor O. Ferreira, Toni El Geitani, Daniel Silva, Bruno Blais, and Gabriela C. Lopes. In-depth validation of unresolved cfd-dem simulations of liquid fluidized beds. *Powder Technology*, 426:118652, 2023. ISSN 0032-5910. doi: <https://doi.org/10.1016/j.powtec.2023.118652>. URL <https://www.sciencedirect.com/science/article/pii/S0032591023004369>.
640
- [5] Bruno Blais and Franois Bertrand. Cfd-dem investigation of viscous solidliquid mixing: Impact of particle properties and mixer characteristics. *Chemical Engineering Research and Design*, 118:270–285, 2017. ISSN 0263-8762. doi: <https://doi.org/10.1016/j.cherd.2016.12.018>. URL <https://www.sciencedirect.com/science/article/pii/S0263876216304981>.
645
- [6] G. G. JOSEPH, R. ZENIT, M. L. HUNT, and A. M. ROSENWINKEL. Particlewall collisions in a viscous fluid. *Journal of Fluid Mechanics*, 433:329346, 2001. doi: 10.1017/S0022112001003470.
- [7] Thomas Roessler and Andr Katterfeld. Dem parameter calibration of cohesive bulk materials using a simple angle of repose test. *Particuology*, 45:105–115, 2019. ISSN 1674-2001. doi: <https://doi.org/10.1016/j.partic.2018.08.005>. URL <https://www.sciencedirect.com/science/article/pii/S1674200119300033>.
650
- [8] Mohammadreza Alizadeh, Maryam Asachi, Mojtaba Ghadiri, Andrew Bayly, and Ali Hassanpour. A methodology for calibration of dem input parameters in simulation of segregation of powder mixtures, a special
655

focus on adhesion. *Powder Technology*, 339:789–800, 2018. ISSN 0032-5910. doi: <https://doi.org/10.1016/j.powtec.2018.08.028>. URL <https://www.sciencedirect.com/science/article/pii/S0032591018306442>.

- 660 [9] Torsten Grger and Andr Katterfeld. On the numerical calibration of discrete element models for the simulation of bulk solids. In W. Marquardt and C. Pantelides, editors, *16th European Symposium on Computer Aided Process Engineering and 9th International Symposium on Process Systems Engineering*, volume 21 of *Computer Aided Chemical Engineering*, pages 533–538. Elsevier, 2006. doi: [https://doi.org/10.1016/S1570-7946\(06\)80100-8](https://doi.org/10.1016/S1570-7946(06)80100-8). URL <https://www.sciencedirect.com/science/article/pii/S1570794606801008>.
- [10] Andrew Phillip Grima and Peter Wilhelm Wypych. Development and validation of calibration methods for discrete element modelling. *Granular matter*, 13(2):127–132, 2011. ISSN 1434-5021.
- 670 [11] Akwasi A Boateng. *Rotary Kilns: Transport Phenomena and Transport Processes*. Elsevier Science, Oxford, 2015. ISBN 9780128038536.
- [12] C. R. Jones, A. Corona, C. Amador, and P. J. Fryer. Dynamics of fabric and dryer sheet motion in domestic clothes dryers. *Drying Technology*, 40(10):2087–2104, 2022. doi: 10.1080/07373937.2021.1918706. URL <https://doi.org/10.1080/07373937.2021.1918706>.
- 675 [13] Gene R. Woodle and James M. Munro. Particle motion and mixing in a rotary kiln. *Powder Technology*, 76(3):241–245, 1993. ISSN 0032-5910. doi: [https://doi.org/10.1016/S0032-5910\(05\)80004-X](https://doi.org/10.1016/S0032-5910(05)80004-X). URL <https://www.sciencedirect.com/science/article/pii/S003259100580004X>.
- 680 [14] Anders Rooma Nielsen, Rasmus Wochnik Aniol, Morten Boberg Larsen, Peter Glarborg, and Kim Dam-Johansen. Mixing large and small par-

- ticles in a pilot scale rotary kiln. *Powder Technology*, 210(3):273–280, 2011. ISSN 0032-5910. doi: <https://doi.org/10.1016/j.powtec.2011.03.029>. URL <https://www.sciencedirect.com/science/article/pii/S0032591011001446>.
685
- [15] Trevor G. Parsons, Jacob H. Masliyah, and Murray R. Gray. Solid-liquid mass transfer in a rotary drum. *The Canadian Journal of Chemical Engineering*, 79(5):726–731, 2001. doi: <https://doi.org/10.1002/cjce.5450790504>. URL <https://onlinelibrary.wiley.com/doi/abs/10.1002/cjce.5450790504>.
690
- [16] Xinxin Tang, Yuanhe Yue, Shuai Wang, and Yansong Shen. Modelling of gas-solid-liquid flow and particle mixing in a rotary drum. *Powder Technology*, 409:117758, 2022. ISSN 0032-5910. doi: <https://doi.org/10.1016/j.powtec.2022.117758>. URL <https://www.sciencedirect.com/science/article/pii/S0032591022006519>.
695
- [17] Paul W. Cleary, Sharen J. Cummins, Matt D. Sinnott, Gary W. Delaney, and Rob D. Morrison. Advanced comminution modelling: Part 2 - mills. *Applied Mathematical Modelling*, 88:307–348, 2020. ISSN 0307-904X. doi: <https://doi.org/10.1016/j.apm.2020.06.048>. URL <https://www.sciencedirect.com/science/article/pii/S0307904X20303231>.
700
- [18] Vladislav Lvov and Leonid Chitalov. Semi-autogenous wet grinding modeling with cfd-dem. *Minerals*, 11(5), 2021. ISSN 2075-163X. doi: [10.3390/min11050485](https://doi.org/10.3390/min11050485). URL <https://www.mdpi.com/2075-163X/11/5/485>.
- [19] Toni El Geitani, Shahab Golshan, and Bruno Blais. Toward high-order cfd-dem: Development and validation. *Industrial & Engineering Chemistry Research*, 62(2):1141–1159, 2023. doi: [10.1021/acs.iecr.2c03546](https://doi.org/10.1021/acs.iecr.2c03546). URL <https://doi.org/10.1021/acs.iecr.2c03546>.
705

- [20] R Di Felice. The voidage function for fluid-particle interaction systems.
710 *International journal of multiphase flow*, 20(1):153–159, 1994. ISSN 0301-9322.
- [21] P. G. Saffman. The lift on a small sphere in a slow shear flow.
Journal of Fluid Mechanics, 22(2):385–400, jun 1965. doi: 10.1017/s0022112065000824.
- 715 [22] P. G. Saffman. The lift on a small sphere in a slow shear flow - corrigendum. *Journal of Fluid Mechanics*, 31(3):624–624, feb 1968. doi: 10.1017/s0022112068999990.
- [23] R. Mei. An approximate expression for the shear lift force on a spherical particle at finite reynolds number. *International Journal of Multiphase*
720 *Flow*, 18(1):145–147, jan 1992. doi: 10.1016/0301-9322(92)90012-6.
- [24] Clayton T. Crowe, John D. Schwarzkopf, Martin Sommerfeld, and Yutaka Tsuji. *Multiphase Flows with Droplets and Particles*. CRC Press, aug 2011. doi: 10.1201/b11103.
- [25] S. I. Rubinow and Joseph B. Keller. The transverse force on a spinning
725 sphere moving in a viscous fluid. *Journal of Fluid Mechanics*, 11(3):447459, 1961. doi: 10.1017/S0022112061000640.
- [26] J. J. Derksen. Numerical simulation of solids suspension in a stirred tank. *AIChE Journal*, 49(11):2700–2714, 2003. doi: <https://doi.org/10.1002/aic.690491104>. URL [https://aiche.onlinelibrary.wiley.com/doi/abs/](https://aiche.onlinelibrary.wiley.com/doi/abs/10.1002/aic.690491104)
730 [10.1002/aic.690491104](https://aiche.onlinelibrary.wiley.com/doi/abs/10.1002/aic.690491104).
- [27] L.W Rong, K.J Dong, and A.B Yu. Lattice-boltzmann simulation of fluid flow through packed beds of uniform spheres: Effect of porosity. *Chemical engineering science*, 99:44–58, 2013. ISSN 0009-2509.

- [28] Hamid Reza Norouzi. *Coupled CFD-DEM Modeling : Formulation, Implementation and Application to Multiphase Flows*. Wiley, Newark, 1. edition, 2016. ISBN 1119005256.
- [29] Yanjie Li, Yong Xu, and Colin Thornton. A comparison of discrete element simulations and experiments for sandpiles composed of spherical particles. *Powder Technology*, 160(3):219–228, 2005. ISSN 0032-5910. doi: <https://doi.org/10.1016/j.powtec.2005.09.002>. URL <https://www.sciencedirect.com/science/article/pii/S0032591005004079>.
- [30] C. A. Cerdeira, E. Carballo, C. A. Tovar, and L. Roman. Thermodynamic properties of aqueous carbohydrate solutions. *Journal of Chemical & Engineering Data*, 42(1):124–127, 1997. doi: 10.1021/jc960168t. URL <https://doi.org/10.1021/jc960168t>.
- [31] V.R.N. Telis, J. Telis-Romero, H.B. Mazzotti, and A.L. Gabas. Viscosity of aqueous carbohydrate solutions at different temperatures and concentrations. *International Journal of Food Properties*, 10(1):185–195, 2007. doi: 10.1080/10942910600673636. URL <https://doi.org/10.1080/10942910600673636>.
- [32] Bruno Blais, Lucka Barbeau, Valérie Bibeau, Simon Gauvin, Toni El Geitani, Shahab Golshan, Rajeshwari Kamble, Ghazaleh Mirakhori, and Jamal Chaouki. Lethe: An open-source parallel high-order adaptative cfd solver for incompressible flows. *SoftwareX*, 12:100579–, 2020. ISSN 2352-7110.
- [33] Toni El Geitani, Shahab Golshan, and Bruno Blais. A high order stabilized solver for the volume averaged navier-stokes equations. *International Journal for Numerical Methods in Fluids*, n/a(n/a), 2023. doi: <https://doi.org/10.1002/fld.5182>. URL <https://onlinelibrary.wiley.com/doi/abs/10.1002/fld.5182>.

- 760 [34] Toni El Geitani and Bruno Blais. Quadrature-Centered Averaging Scheme
for Accurate and Continuous Void Fraction Calculation in Computational
Fluid Dynamics–Discrete Element Method Simulations. *Industrial & En-*
gineering Chemistry Research, mar 2023. doi: 10.1021/acs.iecr.3c00172.
- [35] E. Loth. Lift of a spherical particle subject to vorticity and/or spin. *AIAA*
765 *Journal*, 46(4):801–809, 2008. doi: 10.2514/1.29159. URL [https://doi.](https://doi.org/10.2514/1.29159)
[org/10.2514/1.29159](https://doi.org/10.2514/1.29159).

Appendix A. Values of the Angle of Inclination for the Experiments And Simulations

The tables below summarize the angle of inclination in the rolling regime for
770 the rotary kiln cases in both experiments and simulations. The dashes in the
table represent a change from the rolling regime where an angle of inclination
can no longer be measured.

		Motor Frequency (Hz)									
		20		60		140		200		300	
Particle Type	Fluid Type	Exp.	Sim.	Exp.	Sim.	Exp.	Sim.	Exp.	Sim.	Exp.	Sim.
ABS (5.95 mm)	Air	23	23	26	26	27	27	29	29	30	30
	Water	26	24	27	26	29	29	32	33	33	35
	Sucrose										
	50 %	27	24	29	27	31	31	33	33	-	-
	66.66 %	27	25	30	29	31	31	33	33	-	-
	100 %	32	28	38	34	-	-	-	-	-	-
Glass (3 mm)	Air	28	28	31	30	39	39	-	-	-	-
	Water	29	28	32	31	36	35	-	-	-	-
	Sucrose										
	50 %	31	29	35	34	44	-	-	-	-	-
	66.66 %	31	29	36	35	44	-	-	-	-	-
	100 %	32	31	41	38	-	-	-	-	-	-
Glass (5 mm)	Air	30	28	31	31	35	35	-	-	-	-
	Water	30	30	35	32	38	38	-	-	-	-
	Sucrose										
	50 %	32	29	35	33	36	38	-	-	-	-
	66.66 %	33	29	37	34	-	-	-	-	-	-
	100 %	32	30	-	-	-	-	-	-	-	-

Table A.9: Inclination angle comparison between experiments and simulations for Q2-Q1 simulations.

		Motor Frequency (Hz)									
		20		60		140		200		300	
Particle Type	Fluid Type	Exp.	Sim.	Exp.	Sim.	Exp.	Sim.	Exp.	Sim.	Exp.	Sim.
ABS (5.95 mm)	Air	23	24	26	26	27	27	29	29	30	30
	Water	26	26	27	28	29	29	32	33	32	35
	Sucrose										
	50 %	27	28	29	30	31	33	34	33	-	-
	66.66 %	27	28	30	33	31	33	34	33	-	-
	100 %	32	33	38	42	-	-	-	-	-	-
Glass (3 mm)	Air	28	26	31	31	39	39	-	-	-	-
	Water	29	28	32	31	36	36	-	-	-	-
	Sucrose										
	50 %	31	60	35	35	44	-	-	-	-	-
	66.66 %	31	30	36	35	44	-	-	-	-	-
	100 %	32	30	41	41	-	-	-	-	-	-
Glass (5 mm)	Air	30	27	31	30	35	35	-	-	-	-
	Water	30	28	35	34	38	38	-	-	-	-
	Sucrose										
	50 %	32	30	35	35	36	38	-	-	-	-
	66.66 %	33	32	37	36	-	-	-	-	-	-
	100 %	32	31	-	-	-	-	-	-	-	-

Table A.10: Inclination angle comparison between experiments and simulations for Q3-Q2 simulations.